

Weak localisation in graphene flakes

F. V. Tikhonenko, D. W. Horsell, R. V. Gorbachev, and A. K. Savchenko

School of Physics, University of Exeter,

Stocker Road, Exeter, EX4 4QL, U.K.

Abstract

Weak localisation (WL) is a well known phenomenon caused by quantum interference of charge carriers on closed trajectories. The result is a correction to the classical conductivity and a temperature-dependent change of the conductivity with magnetic field, caused by the fact that the field destroys the interference. Studying WL has become a vital tool in understanding the processes that control the phase coherence of carriers. Here we show that WL in graphene—a single layer of carbon atoms—is very different from that in conventional two-dimensional systems. Due to the chiral nature of charge carriers, WL becomes sensitive not only to inelastic scattering of carriers which breaks the phase, but also to a number of unusual elastic scattering mechanisms. We perform measurements of magnetoconductance on samples with different geometry and quality to determine what scattering processes are responsible for the variety of forms WL takes in graphene.

PACS numbers: 73.23.-b, 72.15.Rn, 73.43.Qt

The quantum correction to the conductivity of two-dimensional (2D) systems due to weak localisation (WL) has been studied for more than twenty years [1, 2, 3]. This provided not only a direct demonstration of the wave nature of charge carriers, but also information about the processes of electron dephasing due to inelastic scattering or scattering by magnetic impurities [3]. As magnetic field destroys electron interference on closed trajectories responsible for WL, measurements of low-field magnetoconductance are usually used to detect it. In this well-established field of research it comes as a surprise to discover that WL in a new two-dimensional system, graphene [4], does not follow the standard conventions. The first attempts to measure WL in graphene have produced contradictory results and initiated great interest in understanding what processes control it [5, 6, 7]. Measurements on graphene flakes fabricated by mechanical exfoliation [5] have shown that in some samples WL is strongly suppressed, while in others it is not, and the suppression was attributed to an effective random magnetic field produced by ripples on the graphene surface. In contrast, in a sample fabricated by an alternative, epitaxial method, WL has been distinctly seen, albeit at a single carrier density [7].

The experimental results [7] were analysed using the recent theory [8]. According to this theory, a remarkable feature of WL in graphene is that it is expected to be sensitive not only to inelastic processes controlling the phase breaking, but also to different elastic scattering mechanisms [8, 9, 10]. The reason for this is that charge carriers in graphene are *chiral*, that is, they have an additional spin-like quantum number defining their wavefunction. This is a result of the fact that their quantum state is a superposition of two contributions coming from two nonequivalent crystal sublattices, A and B [11]. This makes WL in graphene sensitive to defects of the crystal lattice that break the A-B symmetry and destroy the interference of carriers within each of the two valleys in k -space. Such defects, characterised by the scattering rate τ_s^{-1} , include ripples, dislocations and atomically sharp defects [5, 10]. Intra-valley WL can also be destroyed by anisotropy of the Fermi surface in k -space, so-called ‘trigonal warping’ [8], characterised by the rate τ_w^{-1} . In the presence of warping, particles with opposite momenta have different energies, and this prevents their interference on closed paths.

There is one elastic process which acts to restore the suppressed interference. This is *inter-valley* scattering, characterised by the rate τ_t^{-1} , which occurs on the defects with size of the order of the lattice spacing a : such defects can change the carrier momentum by the

size of the Brillouin zone $\Delta k \sim 1/a$. As the two valleys have opposite chirality and warping, intervalley scattering is expected to negate the symmetry breaking and warping effects by allowing carriers from different valleys to interfere, even in the presence of large intra-valley scattering rates τ_s^{-1} and τ_w^{-1} .

In this work we aim to test experimentally what factors are responsible for the manifestation of WL in graphene flakes. We study several samples fabricated by mechanical exfoliation, which are different in their quality and dimensions. This allows us to control the relation between the scattering rates and see what effect this produces on the magnetoconductance (MC). Measurements of MC in perpendicular field are complemented by atomic force microscope (AFM) imaging of the samples which gives direct topological information about the defects [12]. The magnetoconductance is measured at different carrier densities controlled by a gate voltage. These include the Dirac (electroneutrality) region where the type of carrier changes from electrons to holes. There is no clear evidence at the moment that WL exists in this region of apparent zero carrier density. The answer to this question can shed light on the widely debated problem about the origin of the minimum conductivity, $\sigma_{\min} \sim 4e^2/h$, in the Dirac point [13].

Our samples are manufactured using the method of mechanical exfoliation [4] (see the details in Supplementary Material [14]). Figure 1 shows the resistance of four samples with different shapes and mobilities: D, F1, F2 and B, each with a typical peak around $V_g = 0$ (the Dirac point). The conductivity of the samples in the Dirac region σ_{\min} varies in the range $(1.3 - 3.6)4e^2/h$. Insets in Fig. 1 demonstrate measurements of the first quantum Hall plateau, which give a clear indication that all samples are single-layer graphene flakes [15]. Sample D is a square flake of low mobility; F1 and F2 are rectangular of similar dimensions and with larger length than D; B is a narrow strip of similar length to F1, F2 but with much smaller width. We expect that the difference in the shape and quality should manifest itself in the shape of the MC. For example, sample F2 has the highest mobility and thus is expected to have the smallest phase-breaking rate τ_ϕ^{-1} . As the edges of the samples are a source of strong inter-valley scattering, the narrowest sample B should show the largest inter-valley scattering rate τ_i^{-1} .

The resistivity of the samples in Fig. 1 shows reproducible mesoscopic fluctuations (also seen as a function of magnetic field B) caused by the fact that the graphene flakes are small (comparable to the dephasing length and therefore expected to demonstrate universal con-

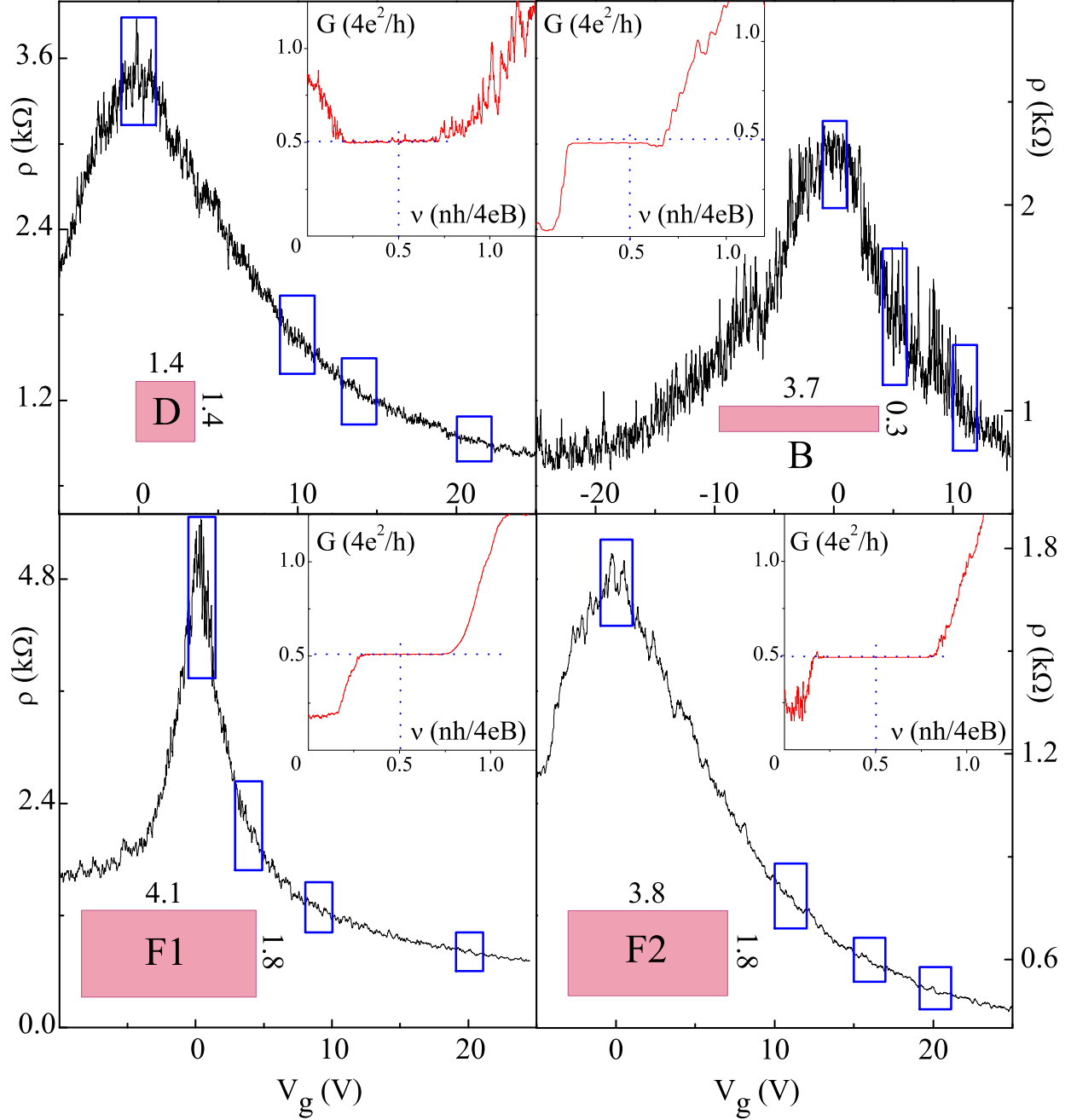


FIG. 1: Resistivity of graphene flakes as a function of carrier density at $T = 0.25$ K. The mobilities (in $\text{cm}^2\text{V}^{-1}\text{s}^{-1}$) of the samples outside the Dirac region: 5100 (D), 8000 (B), 7500 (F1), and 10000 (F2). The sample dimensions are given in μm . The insets show the first quantum Hall plateau.

ductance fluctuations [3]). Therefore, in order to study the conductivity correction caused by WL we used the procedure developed in [16]: $R(V_g)$ is measured at different B and the results are averaged over a range $\Delta V_g = 2$ V shown in Fig. 1 by boxes (for the details, see

[14]). The selected regions are small enough to keep the carrier density constant, but sufficiently large to contain a large number of mesoscopic fluctuations and so provide effective averaging. Examples of the obtained MC in perpendicular magnetic field for different samples are shown in Fig. 2. Although mesoscopic fluctuations are not completely suppressed, the averaged MC curves $\Delta\sigma(B) = \langle\sigma(V_g, B) - \sigma(V_g, 0)\rangle_{\Delta V_g}$ are smooth enough to analyse them in terms of WL. For the analysis of the results we use the theory [8] which predicts that the MC is controlled by several scattering rates, both inelastic (τ_ϕ^{-1}) and elastic (τ_i^{-1} , τ_s^{-1} , τ_w^{-1}):

$$\Delta\sigma(B) = \frac{e^2}{\pi h} \left[F\left(\frac{\tau_B^{-1}}{\tau_\phi^{-1}}\right) - F\left(\frac{\tau_B^{-1}}{\tau_\phi^{-1} + 2\tau_i^{-1}}\right) - 2F\left(\frac{\tau_B^{-1}}{\tau_\phi^{-1} + \tau_i^{-1} + \tau_*^{-1}}\right) \right]. \quad (1)$$

Here $F(z) = \ln z + \psi(0.5 + z^{-1})$, $\psi(x)$ is the digamma function, $\tau_B^{-1} = 4eDB/\hbar$, τ_ϕ^{-1} is the phase-breaking rate and $\tau_*^{-1} = \tau_s^{-1} + \tau_w^{-1}$. (The theory assumes that the momentum relaxation rate τ_p^{-1} is the highest in the system and comes from the Coulomb charges in the SiO₂ substrate and not atomically sharp defects, so that it does not affect the carrier chirality.) Equation 1 gives clear predictions for the shape of the MC depending on the relation between the characteristic scattering rates. In the absence of the warping effect, inter-valley and chirality breaking scattering, $\tau_{i,*}^{-1} \rightarrow 0$, all three functions in Eq. 1 become identical and $\Delta\sigma(B)$ is controlled by the third term and results in *negative* MC, i.e. weak antilocalisation. (Weak antilocalisation was seen earlier in conventional 2D systems, but it was caused by strong spin-orbit interaction and not the chirality of carriers [2, 17]). In the case $\tau_*^{-1} \gg \tau_\phi^{-1} \gg \tau_i^{-1}$ (strong intra-valley but weak inter-valley scattering) the third term is suppressed and the first two fully compensate each other, resulting in *zero* MC. However, if a significant inter-valley scattering is introduced, $\tau_i^{-1} \gtrsim \tau_\phi^{-1}$, the second term becomes smaller than the first, and in small magnetic fields a *positive* MC will be seen. Our results show that the last scenario is applicable to all studied samples: the intra-valley scattering rate τ_*^{-1} is extremely high, but WL is still detectable due to significant inter-valley scattering.

It is clear from Eq. 1 that different relations between the scattering rates should be directly seen from the shape of the experimental curves. Comparing two regions of carrier densities for square sample D in Fig. 2 (Dirac region (a) and electron region (b)) one can see a dramatic difference in the shape of the MC. In (a) the curves have a much stronger downturn, indicating greater importance of the third ('anti-localising') term in Eq. 1 due to smaller rate τ_*^{-1} . Comparison of geometrically similar samples F1 and F2 in Fig. 2(c)

shows that sample F2 (with largest mobility) has a more rapid increase of conductance in smaller field (due to smaller τ_ϕ^{-1}) and more rapid downward turn of the curves at larger fields (due to smaller τ_i^{-1}). It is noticeable that for the narrowest sample B in Fig. 2(d) the MC curves do not turn down at all, indicating a very fast inter-valley rate τ_i^{-1} and therefore unimportance of all terms in Eq. 1 apart from the first.

Figure 3 shows the temperature dependence of the characteristic lengths found from the analysis of the MC by the best fit with Eq. 1. Figure 3(a,b) compares the results for the Dirac and electron regions for sample D. Let us concentrate first on the behaviour of the inelastic dephasing length L_ϕ . The elastic lengths L_i and L_* are seen to be essentially T -independent, as expected, whereas L_ϕ is temperature dependent at high T (≥ 3 K) but saturates at low temperatures. As the length at which L_ϕ saturates is comparable to the size of the sample we attribute this saturation to the fact that the increase of L_ϕ at low T is limited by the sample size. Figure 3(b,d) compares the results for two samples on the same substrate, D and F2, at close values of carrier densities outside the Dirac region. They have different geometries: their widths are close but F2 is about three times longer. One can see that while lengths L_i and L_* are very close in the two samples, the saturation value of L_ϕ at low T is larger in the longer sample F2. This confirms the suggestion that the saturation of L_ϕ at low T is caused by the sample size and not by other mechanisms, such as scattering by magnetic impurities [18].

In the Dirac region a smaller value of the saturation L_ϕ , by $\sim 40\%$, is seen in all studied samples (which is similar to the behaviour of L_ϕ in the electroneutrality region of bilayer graphene [16]). This decrease can be attributed to the formation, at low carrier densities, of disorder-induced electron-hole puddles. At $V_g = 0$ the overall charge in the flake is zero, but in the presence of the puddles this means equal concentration of electrons and holes and not necessarily zero density of each type of carrier. Formation of the puddles separated by p-n junctions with larger resistances than the inner part of the puddle [19] modifies the geometry of conducting paths in the Dirac region and can decrease the effective dimensions of the sample, resulting in a smaller saturation value of L_ϕ .

Figure 3(c) shows the T -dependence of the phase-breaking rate in different regions of sample D. In spite of the expectation that electron-electron interaction in graphene can have an unconventional character [20, 21, 22], our results show that it obeys the usual, linear relation for electron-electron scattering in the ‘dirty limit’, $T\tau_p < 1$: $\tau_\phi^{-1} = \beta k_B T \ln g / (\hbar g)$

[1], where $g = \sigma h/e^2$. (In our samples the parameter $T\tau_p$ varies from 0.002 to 0.4 in the studied temperature range 0.25–25 K.) The empirical coefficient β is found to be between 1 and 2 in all studied regions in Fig. 3(c). It is interesting to note that the larger value $\beta \simeq 2$ (larger phase-breaking rate) occurs in the Dirac region. However, this can be due to some uncertainty in obtaining the value of τ_ϕ in this region from the experimentally determined $L_\phi = (D\tau_\phi)^{1/2}$. (The diffusion coefficient $D = v_F l/2$ is determined from the mean free path l , which in turn is found from the conductivity $\sigma = 2e^2 k_F l/h$.) For the Dirac region, where we suggest the formation of the puddles, the value of the Fermi wavenumber k_F (inside the puddle) is simply estimated at the boundary of the studied region, $|V_g| = 1$ V, Fig. 1.

Now let us discuss the behaviour of the elastic length L_i . We have found that in samples D, F1 and F2 the inter-valley scattering length L_i is comparable to the width of the samples (approximately half the width). This means that the sample edges make a significant contribution to inter-valley scattering. As expected, the narrowest sample B has shown the smallest value of L_i . Surprisingly, however, the value of L_i found for sample B is about five times smaller than the sample width. We have found an explanation of this after AFM examination of this sample which has shown the presence of rapid folds (‘ridges’) across this sample of height ~ 1.5 nm, Fig. 4(a). They are separated by a distance smaller than the sample width and can be another source of inter-valley scattering. Therefore, it is clear that the value of L_i is controlled by both the edges and the defects in the inner part of the sample. (In [7] the MC of a much larger, epitaxial sample gave a small value of $L_i \approx 300$ nm, which we interpret as being due to the fact that this fabrication method produces ~ 200 nm domains [23] that provide an additional source of inter-valley scattering.)

We now compare the lengths L_i and L_* . We can clearly see from Fig. 3 that while L_i is close to the dephasing length, the value of L_* in all samples is significantly smaller and approaches the mean free path. This means that single-valley WL is strongly suppressed. A detailed comparison of L_i and L_* in different regions of carrier density, together with the analysis of the errors in determining them from the MC, is given in the Supplementary Material [14]. The inter-valley length L_i is small in the Dirac region and also at large electron densities. If this decrease at larger densities can be related to an increasing scattering rate due to an increasing density of states, a drop in the Dirac region (similar to the one seen in L_ϕ) remains unexplained. (There could also be an argument against this density of states explanation, as a very similar $L_i(n)$ -dependence was detected in a bilayer system where the

density of states is constant [16].)

It is interesting to understand the microscopic mechanism that can be responsible for the observed large intra-valley scattering rate τ_*^{-1} (small L_*). (We also notice that this rate is generally smaller in the Dirac region than at higher carrier densities.) Scattering by atomically sharp defects is not applicable as an explanation of small L_* : such scattering also produces intervalley transitions, so that L_i and L_* would be comparable. The smaller value of L_* in experiment must therefore be due to an additional scattering rate which affects L_* but not L_i : from warping [8], or from the defects of the crystal structure [5, 10].

Estimation of the expected τ_w^{-1} gives a much smaller rate than the experimental $\tau_*^{-1} \sim 10$ ps⁻¹. In this estimate we used the expression from [8]: $\tau_w^{-1} = 2\tau_p(\mu\epsilon_F^2/\hbar v_F^2)^2$, where ϵ_F is the Fermi energy, $v_F \approx 10^6$ ms⁻¹ is the Fermi velocity and $\mu = \gamma_0 a^2/8\hbar^2$ is the structural parameter ($\gamma_0 \approx 3$ eV is the nearest-neighbour hopping energy and $a \approx 0.26$ nm is the lattice spacing in graphene). In our samples this gives $\tau_w^{-1} \approx 0.3$ ps⁻¹ for the highest measured density and an even smaller rate at lower densities. This means that trigonal warping of the Fermi surface cannot be the main reason of the strong chirality breaking in one valley.

The effect of lattice defects (dislocations) has been estimated using the relation $\tau_s^{-1} = v_F/k_F\xi$, where ξ is the average distance between dislocations [10]. To explain the large value of τ_*^{-1} by these dislocations one would require the typical distance between them to be of the order of 50 nm. Taking into account that the cores of the dislocations should produce an effective inter-valley scattering, the actual distance between them in our samples can be found from the value of L_i , which is more than ten times larger than the estimation of ξ .

The effect of ripples on the graphene surface is also negligible in our samples. According to [5], the effective flux through a ripple of height h and diameter d is $\Phi \sim (\gamma_0/ev_F)h^2/d$. Then the effective magnetic field found from the averaging of random fluxes in the area L_ϕ^2 is $B_{\text{eff}} \sim (\gamma_0/ev_FL_\phi)h^2/d^2$. The roughness of our samples found from AFM measurements, Fig. 4(b,c), is $h \simeq 0.3$ nm and $d \simeq 10$ nm, which gives for a typical $L_\phi \approx 1$ μ m a magnetic field $B_{\text{eff}} \sim 1$ mT which is a small correction to the real fields used in experiment, Fig. 2.

In summary, we have shown that studying weak localisation in graphene systems is a sensitive tool for discovering the details of scattering mechanisms, both inelastic and elastic. Our study has given the following main results. (a) MC due to WL is observed in all samples and at all studied carrier densities, including the Dirac region. Although the MC in the Dirac region is well described by theory [8], the obtained characteristic lengths L_ϕ

and L_i are systematically smaller than at larger carrier density. We relate the decrease of L_ϕ to the formation of electron–hole puddles. The presence of the puddles can then account for the finite value of the conductivity σ_{\min} seen in the Dirac region. (b) In spite of the expectation of unusual electron-electron interaction in graphene [20, 21, 22], the dephasing rate in all samples is found to be well described by conventional theory [1]. (c) The intra-valley WL is shown to be strongly suppressed in all samples, not by trigonal warping but most probably by chirality-breaking defects of the crystal structure. However, we have found that the current models (of ripples and dislocations) cannot explain our observations, and encourage a more detailed theory of intra-valley suppression of WL to be developed. (d) We show that the reason for the observation of WL is the ever present inter-valley scattering, originating from the edges of the sample and partially from imperfections inside it. It can be controlled by changing the sample shape, and total suppression of WL can only be expected in experiments without strong inter-valley scattering, i.e. in large samples without sharp defects in the bulk.

We gratefully acknowledge stimulating discussions with E. McCann, V. V. Cheianov, F. Guinea and V. I. Fal’ko, and thank B. Wilkinson for assistance at an early stage of the experiments.

-
- [1] B. L. Altshuler, D. Khmel'nitzkii, A. I. Larkin, and P. A. Lee, *Phys. Rev. B* **22**, 5142 (1980).
 - [2] G. Bergman, *Phys. Rep.* **107**, 1 (1984).
 - [3] C. W. J. Beenakker, and H. Van Houten, *Solid State Physics* **44**, 1 (edt. by H. Ehrenreich and D. Turnbull, Academic Press Inc., San Diego, 1991).
 - [4] K. S. Novoselov, *et al.*, *Science* **306**, 666 (2004).
 - [5] S. V. Morozov, *et al.*, *Phys. Rev. Lett.* **97**, 016801 (2006).
 - [6] H. B. Heersche, P. Jarillo-Herrero, J. B. Oostinga, L. M. K. Vandersypen and A. F. Morpurgo, *Nature* **446**, 56 (2007).
 - [7] X. Wu, X. Li, Z. Song, C. Berger, and W. A. de Heer, *Phys. Rev. Lett.* **98**, 136801 (2007).
 - [8] E. McCann, *et al.*, *Phys. Rev. Lett.* **97**, 146805 (2006).
 - [9] H. Suzuura, and T. Ando, *Phys. Rev. Lett.* **89**, 266603 (2002).
 - [10] A. F. Morpurgo, and F. Guinea, *Phys. Rev. Lett.* **97**, 196804 (2006).

- [11] T. Ando, T. Nakanishi, and R. Saito, *J. Phys. Soc. Japan* **67**, 2857 (1998).
- [12] M. Ishigami, J. H. Chen, W. G. Cullen, M. S. Fuhrer, and E. D. Williams, *Nano Letters* **7**, 1643 (2007).
- [13] A. K. Geim, and K. S. Novoselov, *Nature Mat.* **6**, 183 (2007).
- [14] Supplementary Material (attached).
- [15] K. S. Novoselov, *et al.*, *Nature* **438**, 197 (2005).
- [16] R. V. Gorbachev, F. V. Tikhonenko, A. S. Mayorov, D. W. Horsell and A. K. Savchenko, *Phys. Rev. Lett.* **98**, 176805 (2007).
- [17] A. K. Savchenko, A. S. Rylik and V. N. Lutskii, *Sov. Phys. JETP* **58**, 1281 (1983).
- [18] F. Pierre, and N. O. Birge, *Phys. Rev. Lett.* **89**, 206804 (2002).
- [19] V. V. Cheianov, and V. I. Falko, *Phys. Rev. B* **74**, 041403(R) (2006).
- [20] J. Gonzalez, F. Guinea, and M. A. H. Vozmediano, *Phys. Rev. Lett.* **77**, 3589 (1996); *Phys. Rev. B* **59**, R2474 (1999).
- [21] S. Das Sarma, E. H. Hwang and W-K. Tse, *Phys. Rev. B* **75**, 121406(R) (2007)
- [22] M. Polini, R. Asgari, Y. Barlas, T. Pereg-Barnea and A. H. MacDonald, arXiv:0704.3786.
- [23] W. A. de Heer, *et al.*, arXiv:0704.0285.

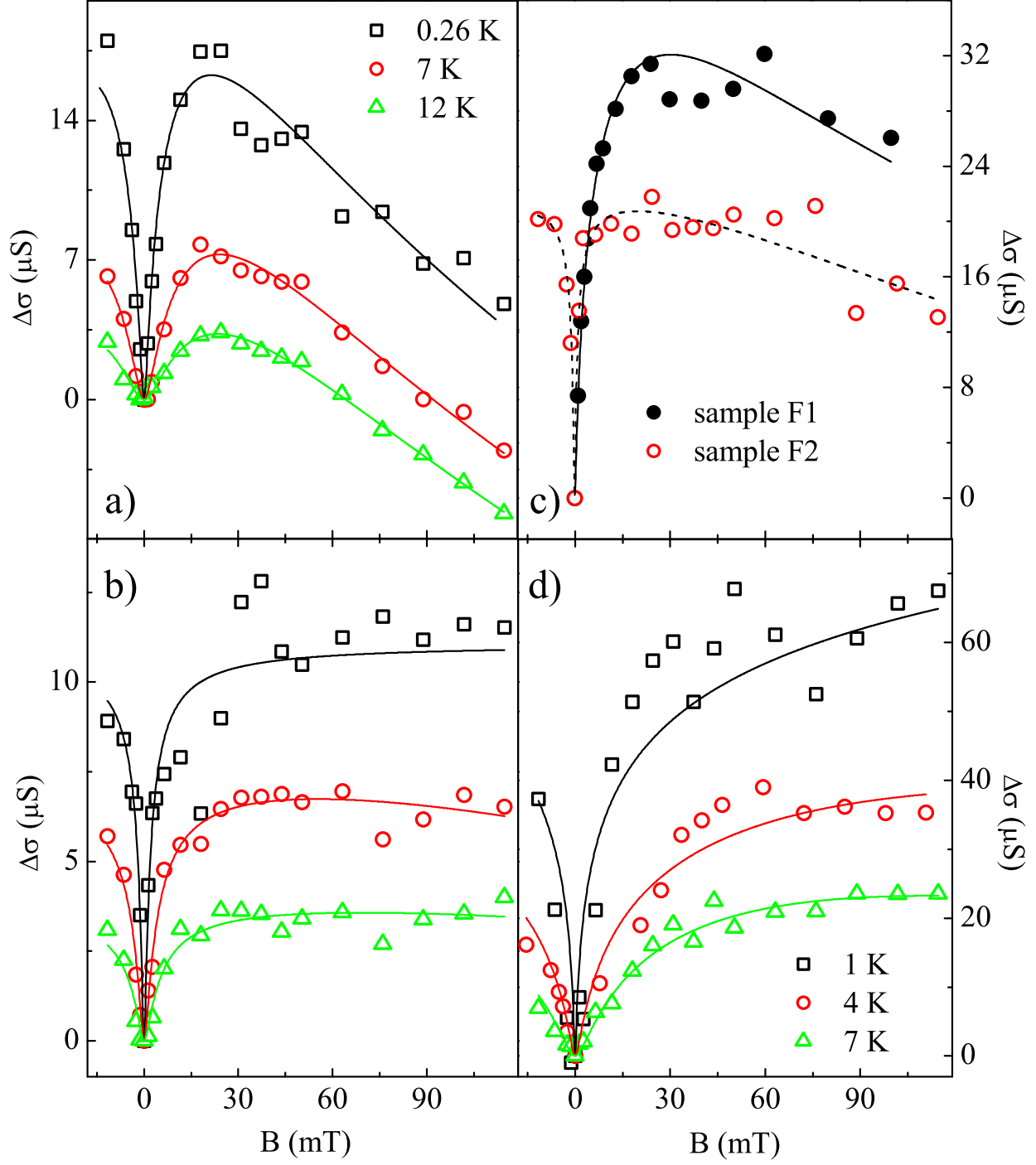


FIG. 2: Magnetoconductivity observed in graphene flakes. (a) Dirac region of sample D, $|V_g| \lesssim 1 \text{ V}$, $n \lesssim 7 \times 10^{10} \text{ cm}^{-2}$; (b) sample D, $V_g \simeq 14 \text{ V}$, $n \simeq 10^{12} \text{ cm}^{-2}$ (the legends of (a) and (b) are the same); (c) samples F1 and F2 at $T = 1 \text{ K}$, $V_g \simeq 10 \text{ V}$, $n \simeq 7 \times 10^{11} \text{ cm}^{-2}$; (d) sample B, $V_g \simeq 11 \text{ V}$, $n \simeq 8 \times 10^{11} \text{ cm}^{-2}$. Lines are best fits to Eq. 1.

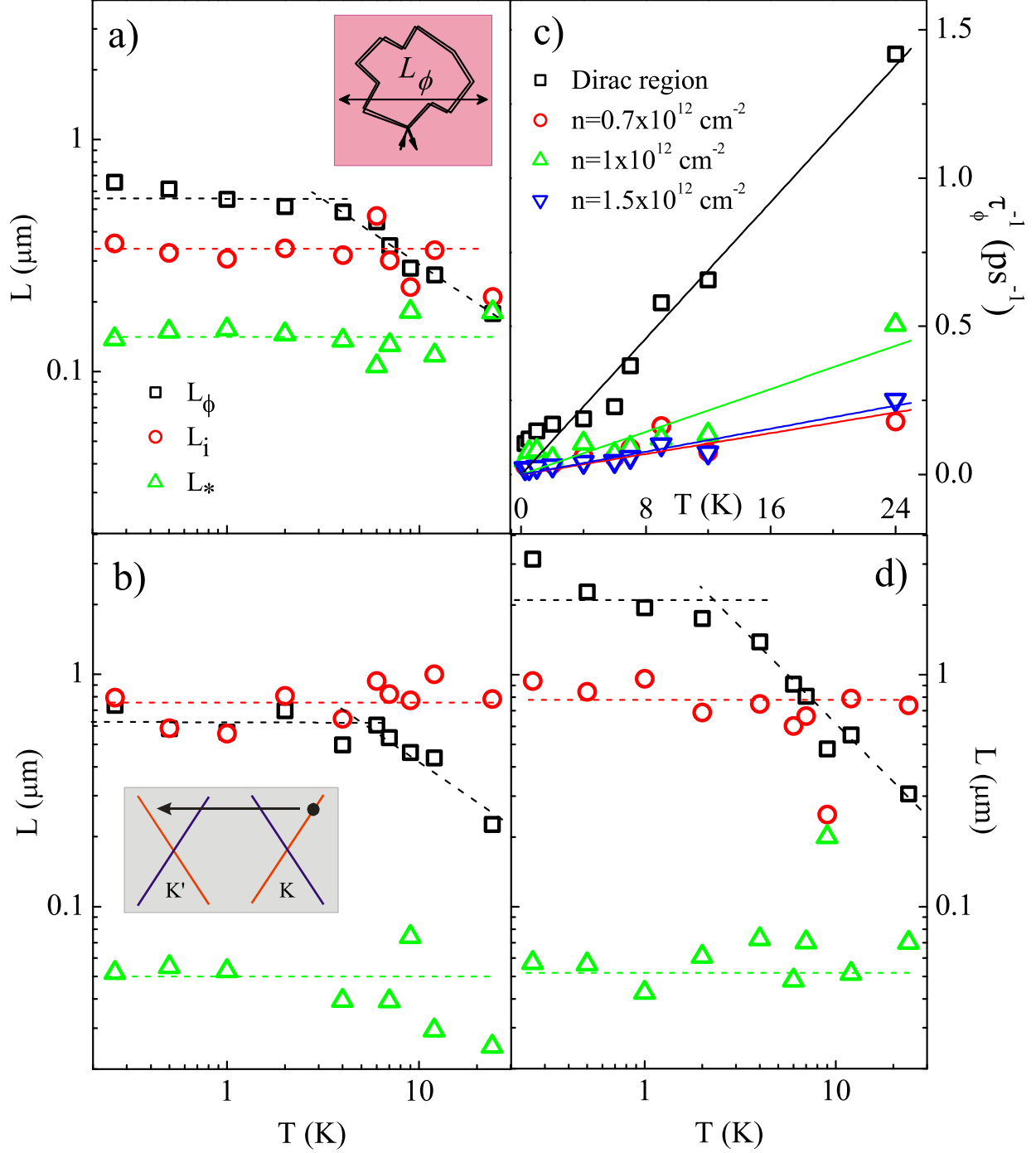


FIG. 3: Characteristic lengths responsible for weak localisation. Sample D: (a) the Dirac region ($n \lesssim 7 \times 10^{10} \text{ cm}^{-2}$) and (b) electron region ($n \simeq 10^{12} \text{ cm}^{-2}$); (c) Phase-breaking rate $\tau_\phi^{-1} = D/L_\phi^2$ as a function of temperature for different carrier densities. Sample F2: (d) Temperature dependence of the characteristic lengths in the electron region ($n \simeq 10^{12} \text{ cm}^{-2}$). Dotted lines are guides to the eye. Inset to (a) illustrates the saturation of L_ϕ at low T due to the sample size. Inset to (b) shows the scattering process behind the length L_i .

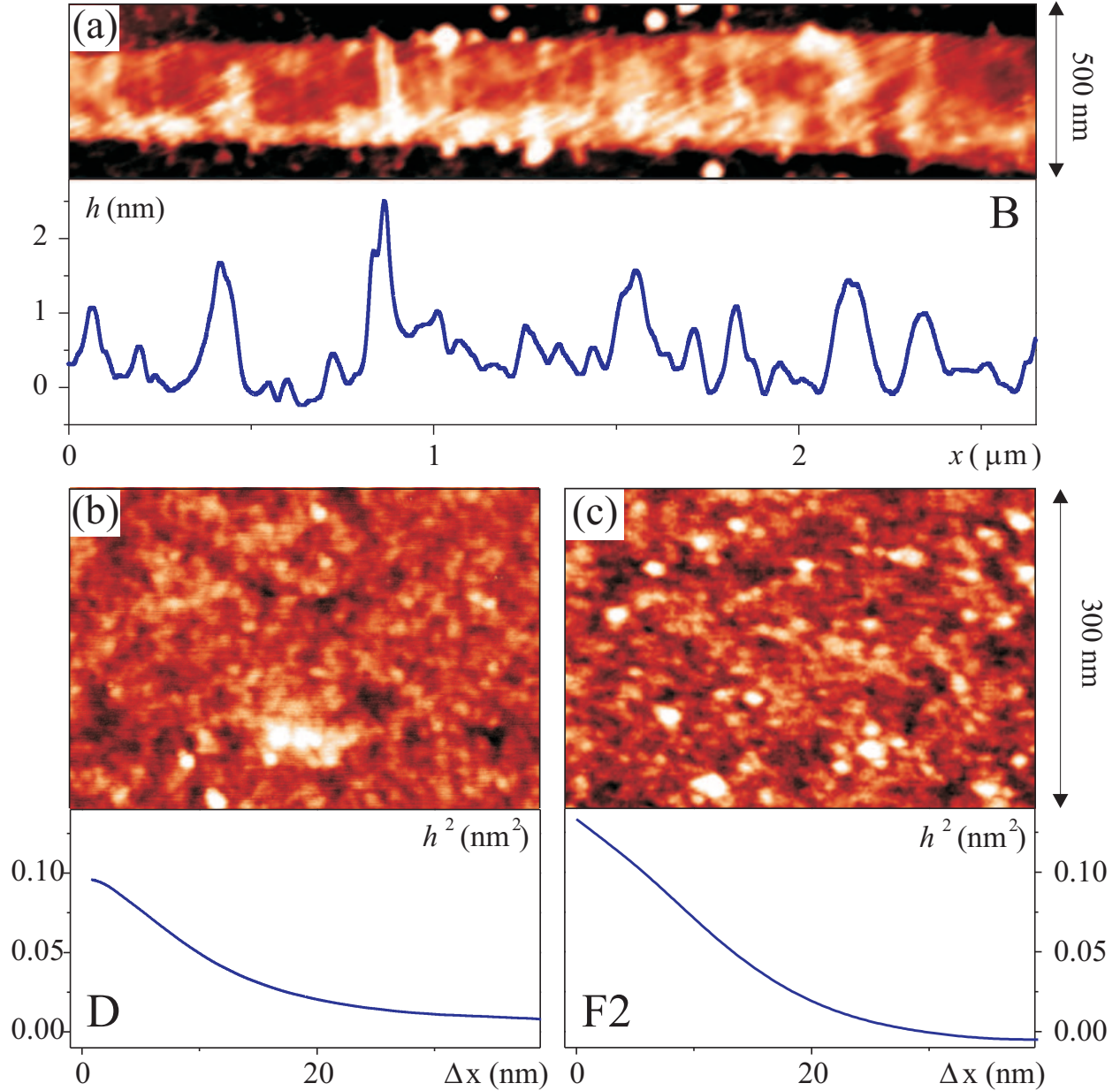


FIG. 4: Atomic force microscope images of graphene surfaces. Below the image of sample B (a) is the surface profile averaged over the width of the sample. Below the images of the topography of samples D (b) and F2 (c) are the corresponding autocorrelation functions of the surface roughness. Samples F2 and D show small, uncorrelated ripples ($d \approx 10$ nm, $h \approx 0.3$ nm) while the surface of B shows distinct ridges of height 1.5 nm. (Details of AFM measurements can be found in [14].)

Weak localisation in graphene flakes: Supplementary material

F. V. Tikhonenko, D. W. Horsell, R. V. Gorbachev, and A. K. Savchenko

School of Physics, University of Exeter, Stocker Road, Exeter, EX4 4QL, U.K.

Samples

Samples were manufactured using the method of mechanical exfoliation of highly-oriented pyrolytic graphite devised in [4], on a $n^+\text{Si}/\text{SiO}_2$ substrate with oxide layer of thickness $t = 300$ nm. Lithographically defined Au/Cr contacts were subsequently made to each flake. Resistance measurements were carried out in the temperature range from 0.25 to 25 K using a standard lock-in technique with 1 nA driving current. Samples B, D, F1 are two-terminal and F2 is four-terminal (the additional contacts were used to account for the contact resistance). The concentration of carriers (electrons n and holes p) in graphene is determined by the capacitance between the graphene and $n^+\text{Si}$ substrate: $e(p - n) = (\epsilon\epsilon_0/t)V_g$. There was a small unintentional doping of the samples leading to a shift in gate voltage (~ 5 V) of the position of the resistance peak with respect to $V_g = 0$, which has been accounted for in the main text. The graphene–Au/Cr contact resistance has been found from the deviation of the height of the quantum Hall plateau from the expected value of $2e^2/h$ (see insets to Fig. 1 of main text). The values of the contact resistance for samples F1 and D are about $\sim 100 \Omega$ and $\sim 600 \Omega$ for sample B.

Averaging procedure and analysis of magnetoconductance

A method of effective averaging is important in small-sized samples to remove the influence of mesoscopic fluctuations, as without it one can get contradictory results for the magnetoconductance (MC). (If we attempt to measure $\Delta\sigma(B)$ at different V_g , the character of the MC depends on the specific point in V_g at which it is measured). Figure 1 shows how the averaging is performed. For each temperature the conductivity of the sample as a function of the gate voltage is first measured across a 2 V range at incremental values of the magnetic field. Then the curve at zero magnetic field is subtracted from each curve and the resulting difference is averaged across the 2 V gate voltage range. One can see from Fig. 1

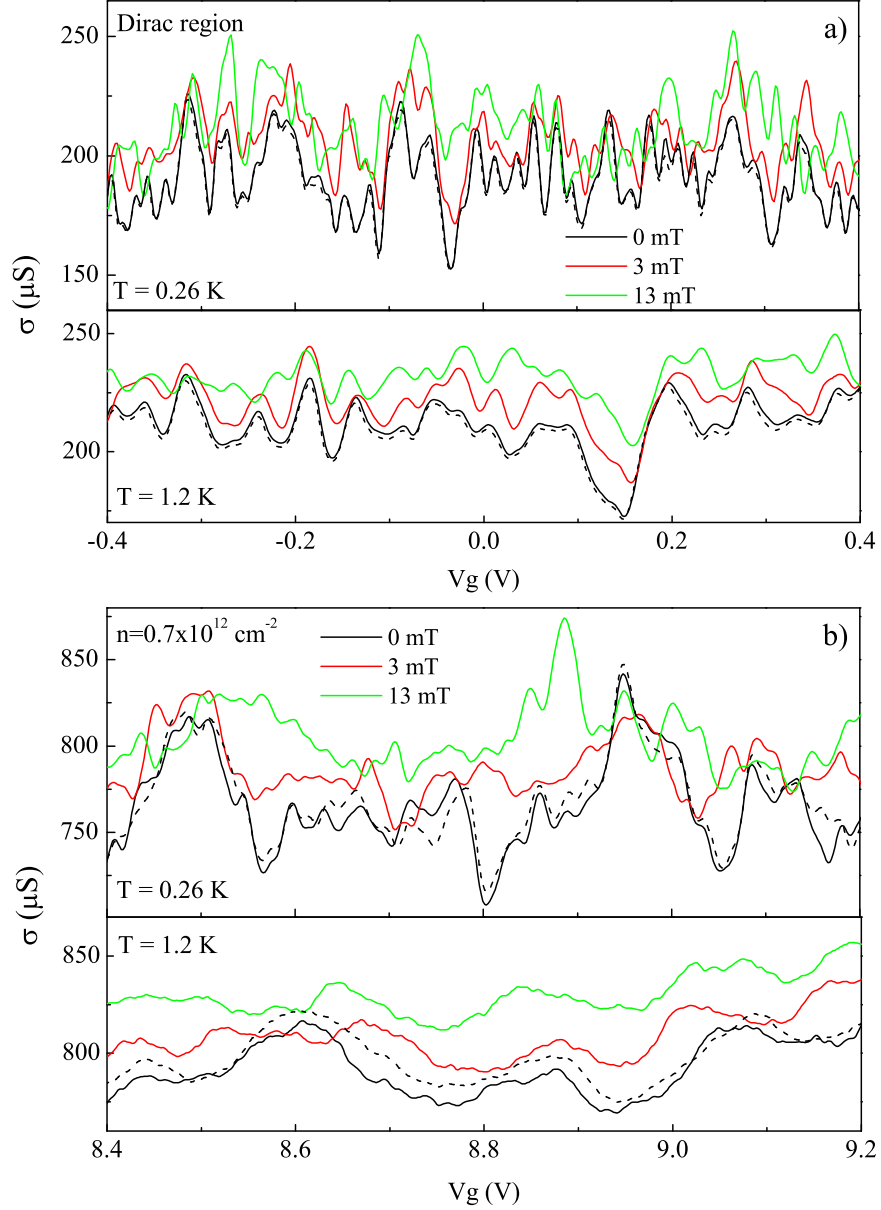


FIG. 1: Illustration of the averaging procedure of the magnetoconductance of sample F1 in two density regions at two temperatures (only a fraction of ΔV_g is shown here): (a) Dirac region, (b) electron region. Dotted lines show repeated sweeps at $B = 0$.

the average increase of $\langle \Delta\sigma \rangle_{\Delta V_g}$ with magnetic field. These averaged values of the MC are plotted as a function of B in Figure 2 of the main text.

The perturbation theory of weak localisation (WL) is applicable at $k_F l \gg 1$ (a diffusive metal). In our samples $k_F l$, found from the conductivity $\sigma = 2e^2(k_F l)/h$, varies in the range 3–30, with the smallest values in the Dirac region: 4, 3, 8 and 6 for samples D, F1, F2 and B,

respectively. Another limitation for the application of the diffusive theory of WL is $B \lesssim B_{\text{tr}}$, where the ‘transport’ magnetic field is found from the condition $L_B = (\hbar/eB)^{1/2} \approx l$. This limited the range of magnetic fields where we perform the analysis to $B \leq 100$ mT.

For the narrowest sample B, the dephasing length is larger than its width and therefore the 1D theory of WL should be used in the analysis of its MC in small fields. However, at fields where $L_B < W$ (W is the width of the sample) i.e. at $B > 7$ mT, the 2D theory becomes applicable. As the bulk of the data is obtained in this range of the field, we have primarily used 2D theory (Eq. 1 in main text) to analyse the MC. (It is interesting to note that using 1D theory in the whole range of the fields still gives good agreement with the shape of the MC of sample B.)

Comparison of characteristic lengths and times

Figure 2 shows for samples F1, F2 and D a comparison of the length L_* with length L_i , as well as the values of the corresponding times τ_* and τ_i (using $L_x = (D\tau_x)^{1/2}$) for different carrier densities. We emphasise that in the analysis of the MC the value of L_* is closely linked to that of L_i . In Eq. 1 the second and third terms have the same sign, therefore by a slight increase of one of them and a corresponding decrease of the other, one can get a similar agreement with experiment. Figure 2 shows not only the values found from the best fit (the higher B -region being most sensitive to these two parameters) but also the synchronous variation allowed in these values while retaining a good fit, indicated by arrows. In spite of the variations, there are several trends seen in the figure. First, the value of L_i is always significantly larger than L_* and somewhat larger in the better quality sample F2. Second, there is a decrease of L_i with increasing carrier density, although its value is smaller in the Dirac region. Finally, there is a decrease of L_* when the carrier density is increased above the Dirac region. The dashed curves in Fig. 2 indicate the expected decrease of L_i and τ_i if the scattering rate is proportional to the density of states, which increases linearly with the Fermi energy $\epsilon_F \propto V_g^{1/2}$.

Estimations of the effects suppressing WL in a single valley

Trigonal warping

According to [8] the breaking of the time-reversal symmetry in one valley can occur due to the suppression of backscattering by the trigonal warping of the Fermi surface. The trigonal

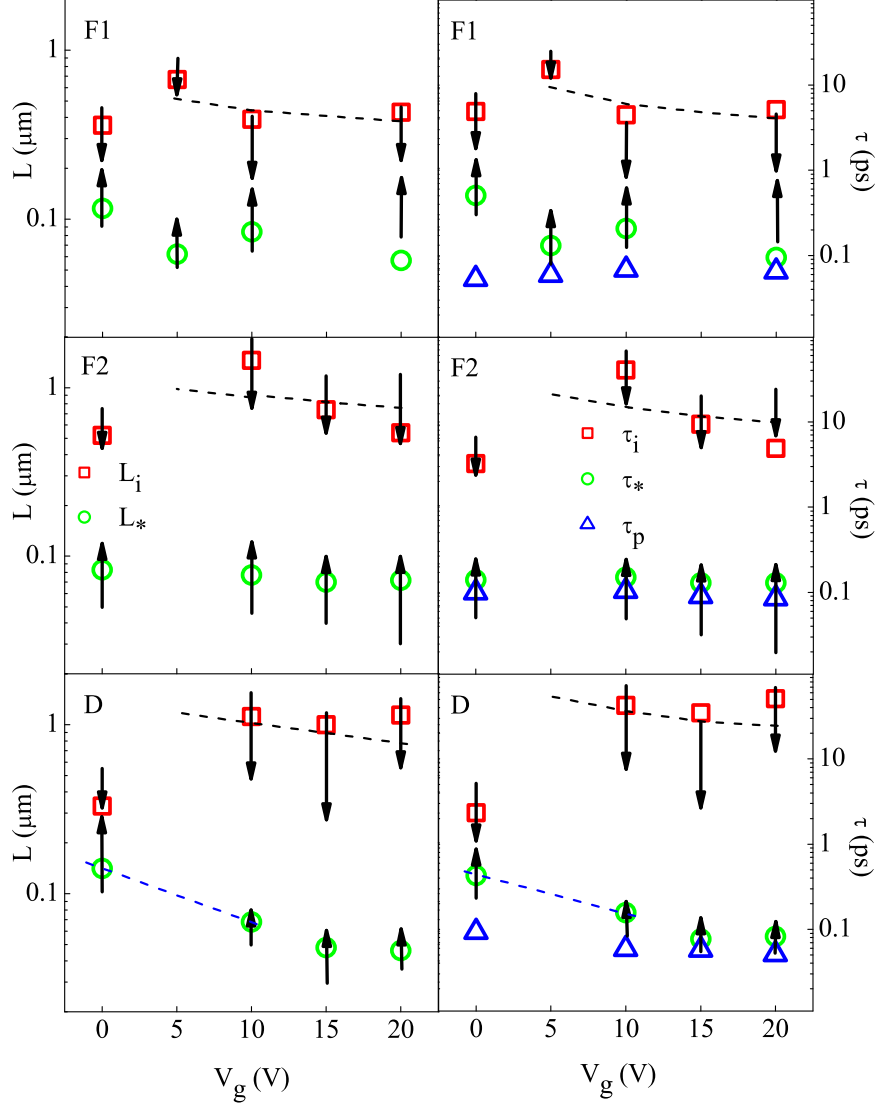


FIG. 2: Comparison of characteristic lengths and times for samples F1, F2 and D at different carrier densities.

warping rate is

$$\tau_w^{-1} = 2\tau_p(\mu\epsilon_F^2/\hbar v_F^2)^2,$$

where τ_p is the momentum relaxation time, $v_F \approx 10^6 \text{ ms}^{-1}$ is the Fermi velocity and μ is the structural parameter equal to $\mu = \gamma_0 a^2 / 8\hbar^2$. Here $\gamma_0 \approx 3 \text{ eV}$ is the nearest-neighbour hopping energy and $a \approx 0.26 \text{ nm}$ is the lattice constant in graphene. For the typical parameters in our samples we obtain $\tau_w^{-1} \approx 0.001 \text{ ps}^{-1}$ for the Dirac region ($\epsilon_F \approx 30 \text{ meV}$, $\tau_p \approx 0.1 \text{ ps}$) and $\tau_w^{-1} \approx 0.3 \text{ ps}^{-1}$ for the highest measured concentration ($\epsilon_F \approx 130 \text{ meV}$, $\tau_p \approx 0.05 \text{ ps}$). Trigonal warping of the Fermi surface is therefore a very weak effect compared to other intra-

valley scattering mechanisms and cannot be the main reason of the strong chirality-breaking observed in our experiments ($\tau_*^{-1} \approx \tau_p^{-1}$).

Dislocations

Another possible mechanism of chirality breaking in the graphene sheet is dislocations in the honeycomb lattice [10]. If the trajectory of a quasiparticle goes near the core of a dislocation it leads to a change of the phase due to the induced strain. For randomly distributed dislocations the scattering rate related to this mechanism is

$$\tau_{\text{gauge}}^{-1} \approx \frac{v_F}{k_F \xi},$$

where ξ is the average distance between dislocations [10]. In order to obtain the experimentally found chirality-breaking rate $\tau_*^{-1} \approx 10 - 20 \text{ ps}^{-1}$ the distance ξ should be about 15 – 50 nm. However, the cores of the dislocations should also cause inter-valley scattering, which is why this estimation is in contradiction with the relatively large value of the inter-valley scattering length ($L_i \approx 1 \mu\text{m}$) observed experimentally.

Ripples

As proposed in [5], ripples in the graphene layer on a silica substrate can lead to suppression of weak localisation because of the effective magnetic field generated by strain of the interatomic bonds. The vector potential corresponding to a single ripple with diameter d and height h is [5]:

$$A = \frac{\gamma_0 |\nabla h|^2}{ev_F},$$

where $\nabla h \approx h/d$. The flux through one ripple is $\Phi = \oint \mathbf{A} \cdot d\mathbf{l} \approx Ad$ and $\Phi = \int \mathbf{B} \cdot d\mathbf{S} \approx Bd^2$, therefore the magnetic field associated with one ripple is

$$B \approx \frac{A}{d} = \frac{\gamma_0}{ev_F} \frac{h^2}{d^3}.$$

Since the curvature vector of a ripple is random, the resulting magnetic field through the area limited by the dephasing length L_ϕ and containing $N \approx L_\phi^2/d^2$ ripples should be averaged as follows:

$$B_{\text{eff}} = \frac{B}{\sqrt{N}} = \frac{\gamma_0}{ev_F L_\phi} \left(\frac{h}{d}\right)^2.$$

The roughness of the graphene sheet found from AFM measurements is about 0.3 nm and the size of the features is about 10 nm. This gives a value for the magnetic field associated

with one ripple $B \sim 0.1$ T. For our typical value of $L_\phi \sim 1 \mu\text{m}$ the effective magnetic field is then $B_{\text{eff}} \sim 1$ mT. Since suppression of the quantum interference requires a magnetic field $B_{\text{eff}} > B_{\text{tr}} \sim 0.1$ T, the estimated value is too small to destroy the localisation effect. The random magnetic field can only introduce an uncertainty in the value of B , Fig. 2 of the main text, comparable to the accuracy to which the field is set by the power supply.

Potential gradients

The last mechanism which can produce the breaking of time-reversal symmetry is a gradient of potential coming from the charged impurities in the substrate. A potential gradient leads to a distortion of the dispersion curve of a single valley and hence breaks the valley symmetry. As shown in [10] the resulting scattering rate can be estimated as

$$\tau_{\text{grad}}^{-1} \approx \tau_p^{-1} (k_F a)^2 .$$

In order to get $\tau_{\text{grad}}^{-1} \approx \tau_p^{-1}$ one should have $k_F a \approx 1$. This corresponds to the carrier density $n = k_F^2/\pi \approx 5 \cdot 10^{14} \text{ cm}^{-2}$, which is two orders of magnitude higher than the densities studied in the experiment.

We conclude from these calculations that all existing estimations for the chirality-breaking scattering rates are not sufficient to explain our experimental results.

Scanning probe microscopy studies

The atomic force microscope used in this work was an Ntegra Aura from NT-MDT. We used non-contact tips NSG01 with resonance of 150 Hz at an amplitude of $\lesssim 40$ nm. To obtain high resolution in the xy -plane ‘diamond-like carbon’ coated tips with curvature radius 1 – 3 nm were used; tip convolution therefore limited feature resolution to this scale. To remove the influence of the water layer present on the silica substrate all measurements were performed in an atmosphere of dry nitrogen at 3 mbar, giving a tip resonance quality factor $Q \approx 1000$. The noise in the z -scale (height) is of the order 0.02 nm measured on pure graphite and silica with the AFM operating with acoustic and vibrational isolation.

We found that the surfaces of the silica and the graphene after lithographic processing were covered in droplets of PMMA with height ≈ 2 nm, similar to the findings of [12]. They reduced the image quality and also made determination of the step edge between graphene and silica difficult. To obtain the scans of clean graphene shown in Fig. 4 of the main text

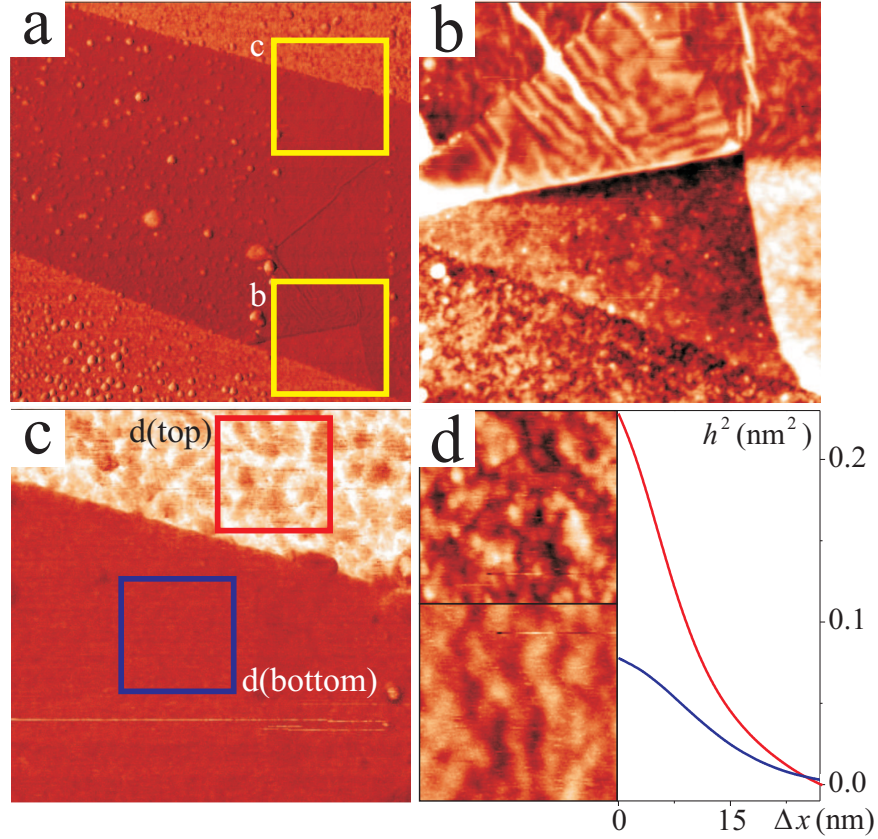


FIG. 3: AFM measurements of sample F2. (a) Phase contrast image where the PMMA droplets on the left and cleaned area on the right can be seen, with two regions in the clean area highlighted by boxes. (b) Magnified topographic image of box ‘(b)’ showing the torn edge of the graphene flake. (c) Magnified phase contrast image of box ‘(c)’ with silica (top) and graphene (bottom). (d) Autocorrelation analysis of the roughness in the boxes highlighted in (c), with insets of silica (top) and graphene topography (bottom). Scan (a) is $3\ \mu\text{m}$ size and the phase change at the graphene–silica boundary is 2° . Scans (b)–(c) have the same $0.8\ \mu\text{m}$ size. In (b) the colour-scale varies over 4 nm.

we mechanically cleaned the surfaces. Figure 3(a) shows a phase contrast image of sample F2 where both the PMMA droplets and a cleaned area are seen.

To understand the extent to which the PMMA droplets exist under the flake (due to the lithographic process of depositing location markers prior to the deposition of the graphene flake), we introduced a tear and fold into the sample F2 as seen in Fig. 3(b). We see first that the surface under the flake is indeed free from PMMA droplets and therefore the topography of the flake is only influenced by the silica roughness. (This conclusion was

also confirmed by similar measurements on other flakes). Having a flake fold allows us to determine better the thickness of the flake, by measuring the step height between two graphene areas (as opposed to measurements of the step height between silica and graphene which always give a larger value of the step, ~ 1 nm). We find that the thickness of the flake is < 0.5 nm, which confirms that the flake is a monolayer (supporting the results of the quantum Hall measurements discussed in the main text). An interesting result from the tear is that the graphene flake has a tendency to form larger ripples when detached from the silica surface, with a ripple height ~ 0.5 nm and width 20 nm. (The roughness of the flake on the substrate is ~ 0.3 nm, see the main text.) When comparing the surface roughness of silica and graphene, Fig. 3(c,d), we see that the surface height variation on the clean silica surface is $\sim 60\%$ larger than on the graphene, i.e. graphene significantly smoothes out the substrate roughness.